Surfaces, Silica and Semivolatile Organics — Limonene Uptake and Desorption Indoors and Outdoors

Journal:	*Environmental Science: Processes & Impacts*
Manuscript ID	EM-ART-04-2025-000275.R1
Article Type:	Paper

Surfaces, Silica and Semivolatile Organics — Limonene Uptake and Desorption Indoors and Outdoors

Ryan S. Reynolds,[1] Kristen N. Johnson,[1,2] Katelyn Pacaud,[1] Michael Ezell,[1]
Pascale Lakey,[1] Manabu Shiraiwa,[1] Barbara J. Finlayson-Pitts[1]

[1] Department of Chemistry, University of California Irvine, Irvine, CA 92697-2025
[2] Department of Chemistry, Tennessee Technological University, Cookeville, TN 38505

For submission to: Environmental Science: Processes & Impacts

Revised and submitted

May 8, 2025

Environmental Significance

The partitioning of semivolatile organic compounds between the gas and condensed phases determines their distribution and chemistry in the environment. Thus, accurate descriptions of the interaction between environmentally-relevant organic gases and surfaces is crucial to modeling atmospheric chemistry both indoors and outdoors. In this study, we measure the uptake and desorption of limonene—a highly reactive compound emitted from both biogenic and anthropogenic sources—from silica surfaces which are ubiquitous in both the natural and built environment. These results show the importance of the properties of both the surface and the gas in partitioning of semivolatile species and provide key parameters for estimating the distribution of limonene across the broad range of temperatures encountered in the atmosphere.

Abstract

Adsorption of organics on surfaces is important in both outdoor and indoor environments. Surfaces can serve as sinks for gas-phase species, act as reservoirs by emitting previously partitioned organics back into the gas phase, and can facilitate heterogeneous chemistry. We report here studies of the uptake and desorption energetics of gas-phase limonene, a volatile and widely-distributed monoterpene, on solid silica nanoparticles using a unique apparatus that allows for temperature programmed desorption (TPD) measurements of surface binding energies as well as Knudsen cell gas uptake measurements. A multiphase kinetic model was applied to these data to provide additional molecular-level understanding of the processes involved. TPD experiments yielded an average desorption energy of 47.5 ± 8.2 kJ mol^{-1} (±1s, sample standard deviation), the first direct experimental measurement of this parameter over a broad temperature range (150–320 K). Initial net uptake coefficients ($\gamma_{0,net}$) range from $(1.7 \pm 0.3) \times 10^{-3}$ (±1s) at 210 K to $(2.3 \pm 0.4) \times 10^{-4}$ (±1s) at 250 K, reflecting increased rates of desorption with an increase in temperature combined with increased rates of diffusion and re-adsorption within the pores between adjacent silica nanoparticles. Effective Langmuir constants, which also reflect the effects of pore diffusion and re-adsorption, were determined from the uptake data and vary from $(1.8–0.3)\times10^{-13}$ cm^3 $molecule^{-1}$ over the same temperature range. These results are in excellent agreement with previous studies around room temperature and with theoretical calculations of the energetics of the limonene-silica interaction. The strong attraction between limonene and the polar silica surface shows the importance of including such interactions in models of the atmospheric fates of terpenes both indoors and outdoors.

Introduction:

Gas-surface interactions play a central role in many systems, especially those of atmospheric relevance.[1-4] For example, atmospheric gases interact with surfaces both indoors and outdoors,[5-7] resulting in uptake to form adsorbed films[8-11] or chemical reactions that change the composition of the gas and condensed phases in ways that may be deleterious to human health.[12] This can be particularly important in indoor enclosed environments, where humans spend >93% of their time,[13] because surface-to-volume ratios are large and concentrations of trace gases produced by indoor activities (eg human respiration, combustion, cooking) may be relatively high due to poor ventilation in these spaces.[14]

In the atmosphere, the interaction of gases with airborne particles leads to gas incorporation into the particle and subsequent particle growth. When Particles grow to ~100 nm in diameter they can efficiently scatter light[15-17] and serve as cloud condensation nuclei, two processes that impact climate.[18-22] This is also the size range that reaches the alveolar region of the lung and may cause deleterious health effects.[23-32] For example, airborne particles have well-known negative health impacts on the lung, heart and reproductive systems as well as on neurodegenerative diseases.[33-36] As a result, understanding the processes that grow particles in air or form surface films at a molecular level is critical for ultimately predicting their impacts on climate and health. Gas-surface interactions play fundamental roles in such processes.

Uptake of organics on particle surfaces involves a number of individual steps,[37-39] which together control the net uptake of the organic on the surface under consideration. An illustration of these steps is shown in Figure 1. For those gas-surface collisions that do not result in elastic scattering, the first step is adsorption of the gas onto the particle surface. This is followed by desorption back into the gas phase, or re-distribution within the condensed phase. The relative importance of these processes determines their contribution to particle growth. For example, for highly viscous particles or surface films, diffusion into the bulk is much slower than for liquid particles,[40] and as a result, rates of growth are determined by the relative rates of the uptake and desorption processes. Smaller rates of desorption and hence longer residence times of the adsorbed species on the surface will favor growth, either *via* diffusion into the bulk or via a burying mechanism.[41, 42]

Both adsorption and desorption are determined by the attractive forces between the functional groups of the gas-phase molecule and those on the surface. These forces include London dispersion forces between non-polar molecules, dipole-induced dipole (Debye) forces between polar and non-polar molecules, dipole-dipole attractions and hydrogen-bonding. Thus, the structures and properties of both the surface and the adsorbing gas must be taken into account.

To explore the effects of these interactions in the atmosphere, we examine here the interaction of a common volatile organic compound, limonene, and a common surface material, namely silica. Limonene is found both outdoors, where it is generated by plants,[43] as well as indoors due to its use in cleaning supplies, building materials, cosmetics, fragrances and food.[12, 44-46] Indeed, indoor concentrations can be an order of magnitude or more greater than those outdoors.[47] Limonene is also a chiral molecule having two enantiomers, with the (+) enantiomer typically dominating anthropogenic emissions of limonene due to its preferential use in the manufacturing of volatile chemical products.[43] Once emitted, limonene is highly reactive in air, forming a complex mixture of oxidized products on surfaces[48] as well as secondary organic aerosol particles in air.[49-51] Silica is also found both outdoors and indoors, is a significant component of soils and airborne dust particles[4] and is widely used in the built environment in the form of glass.[52] Thus, the interaction of gaseous limonene and silica surfaces is of interest for both indoor and outdoor chemistry.

There have been previous experimental and theoretical studies of the limonene-silica interaction around room temperature,[7, 48, 53-58] giving a surface accommodation coefficient of 0.96[55] and calculated desorption energies in the range of 42–57 kJ mol^{-1}.[7, 55, 56] These studies established that both dispersion forces and hydrogen bonding between the surface Si-OH groups and the π electrons of the C-C double bonds in limonene contribute to significant uptake, even at room temperature.

Here we report results on the limonene-silica system using a newly developed apparatus[59] that allows both uptake and desorption to be experimentally determined over a wide temperature range (150–320 K). To the best of our knowledge, this represents the first direct experimental measurement of the desorption energy and temperature-dependent net uptake coefficients for limonene from a silica surface well below room temperature. In addition, multiphase kinetic modeling is used to provide molecular-level insight into the limonene-silica interactions. These data are compared to previous measurements of the benzene-silica system[7, 56, 59-61] to provide molecular-level understanding of the gas-surface interactions that can be used in a predictive sense that applies more broadly to other systems.

Experimental:

The experiments were carried out using a unique apparatus combining Knudsen cell and temperature programmed desorption (TPD) capabilities which has been described in detail elsewhere.[59] A schematic diagram of the experiment is reproduced in the SI (Figure S1). Briefly, the apparatus consists of a large, 6-port chamber vacuum-connected to a sample stage that is temperature controlled. Surface samples were prepared by depositing 1 mL of a suspension of fumed silica powder (Cabosil® Grade 5, Cabot Corp.) (average particle size between 200–300 nm) in benzene (EMD Millipore, HPLC Grade) at a concentration of 1 mg/mL on the bottom of a sample cup having either a plasma-cleaned silicon wafer (Si) or copper (Cu) surface. The solvent was evaporated under a stream of N_2 and then the sample was placed in the reaction chamber where it was heated (to 350 K) overnight under vacuum. A fresh surface sample was prepared for each run. Given the high surface area of the silica particles (~ 2000 cm^2) compared to the area of the temperature-controlled surface of the sample cup (13.6 cm^2), the sample cup is not expected to take up significant amounts of limonene and no significant difference is expected between runs on Cu and Si substrates. The limonene ((R)-(+)-Limonene, Aldrich, 97%) was stored over alumina ($Al_2O_{3,}$ Alpha Aesar, 99.99%) to remove oxidized impurities. Prior to experiments, it was transferred to a 50 mL bulb and subjected to at least three freeze-pump-thaw cycles to remove dissolved air.

TPD Experiments: For TPD experiments, the silica powder was first cooled to 150 K using a combination of liquid nitrogen cooling and controlled heating (EFit power supply and 3216 temperature controller, Eurotherm) of the copper stage in contact with the bottom of the sample cup. Gas-phase limonene was admitted through a doser for up to 10 minutes onto the cooled surface. The surface temperature is below the freezing point of limonene, resulting in multilayers of adsorbed limonene molecules. After gas dosing was completed, the adsorbed limonene layer was then annealed by heating to selected temperatures before being cooled back to 150 K. TPD curves were then recorded using mass spectrometry as the sample was heated from 150–320 K using a linear temperature ramp with a heating rate of 0.25 K s^{-1}. The desorbing limonene molecules were detected as mass spectral signal with m/z = 68, which is the most abundant peak in the electron impact ionization mass spectrum of limonene.[62]

Annealing temperatures were varied from 195 K to 240 K to achieve small multilayer or sub-monolayer coverages of limonene prior to TPD. Samples were first annealed at the lowest annealing temperature, which resulted in two peaks appearing during the temperature ramp (multilayer curve, Figure 2), one peak due to desorption from a multilayer and one peak at a higher temperature due to a silica-adsorbed limonene monolayer. The multilayer TPD curve was deconvoluted into two Gaussian curves: one representing the multilayer and a separate Gaussian for the monolayer (dashed line, Figure 2). The integrated area of the second Gaussian curve was taken to represent the total number of limonene molecules adsorbed into the monolayer. During subsequent runs, higher annealing temperatures were chosen such that the multilayer peak disappeared completely during the annealing step, and only TPD curves with sub-monolayer coverages were observed. The area under each sub-monolayer peak was ratioed to that of the monolayer to obtain the fractional coverage (θ) that was initially present (θ_0) at the start of each run.

Uptake Experiments: For measurements of net uptake coefficients, which represent the fraction of gas collisions that lead to adsorption, the doser was replaced by a movable lid which seals off the sample cup from the chamber. With the lid closed, small pressures of limonene were admitted to the cell to obtain I_0, the steady state mass spectral signal at $m/z = 68$ in the absence of uptake on the silica. Over the timescale of these experiments, I_0 was nearly constant. On opening the lid to expose the silica surface, the signal dropped to a minimum value, I_{min}, after which the signal gradually began to recover due to desorption from the surface. The magnitude of the initial drop, combined with the area of the orifice into the mass spectrometer and the area of the silica surface, was used to obtain initial net uptake coefficients, $\gamma_{0,net}$,[4]

$$\gamma_{0,net} = \left(\frac{I_0}{I_{min}} - 1\right)\left(\frac{A_0}{A_s}\right) \qquad \text{(I)}$$

where A_0 is the effective area of the orifice leading from the sample chamber to the mass spectrometer and A_s is the surface area of the silica sample. Unlike the case of reactive uptake, where the gas is irreversibly lost to the surface, limonene simultaneously adsorbed to and desorbed from the surface after initial uptake, and hence the signal gradually increased again until it reached a new apparent steady-state value.

Kinetic Multi-Layer Modeling: Time profiles of the uptake data were simulated using a kinetic multi-layer model, similar to that used to model uptake in a previous system.[38, 59] Briefly, the model used a flux-based approach to describe vertical diffusion through the pores between silica particles and reversible adsorption of limonene to the silica particle surfaces in each layer. The resulting concentrations of limonene in the gas phase, in the pores between silica particles, and on the particle surfaces were calculated as a function of depth and time. A detailed description of the model and a list of model parameters are given in the SI (Table S1).[38, 63] The diffusion coefficient through the pores was then varied until the model closely replicated the experimental measurements. The surface accommodation coefficient ($\alpha_{s,0}$) on an adsorbate free silica surface was set to 1 based on molecular dynamic simulations of small organic molecules interacting with silica and other surfaces at room temperature.[54, 55, 64, 65] A sensitivity test was conducted where $\alpha_{s,0}$ was reduced by up to a factor of 10, and it was found that within this range very similar fittings to the measurements could be obtained by also decreasing the desorption rate constant (k_d) by the same factor.

Results & Discussion:

TPD Experiments: Figure 2 shows typical TPD data for limonene for different annealing temperatures. The shapes of each curve reflects competition between increasing rates of desorption as the temperature rises and decreasing amounts of adsorbed gas as surface coverage decreases with increasing temperature. To interpret and analyze these data, the binding mechanism must be first understood. There are different models of non-reactive gas adsorption depending on the strength of binding of the adsorbate to the surface.[66] For weak binding, the adsorbate can move in the *x-y* plane because the thermal energy is sufficient to overcome the barriers to translation on the surface. This is known as the ideal 2D gas model. For strong binding where the barriers are high relative to the thermal energy, known as the ideal 2D lattice gas model, the adsorbate remains fixed at one location. The intermediate case is that of a hindered translator.

With a relatively high binding energy, limonene is best described by the ideal 2D gas lattice model. As discussed in detail by Campbell and coworkers,[66] the rate of desorption should vary as

$[\theta/(1-\theta)]$ $\exp(-E_d/RT)$ where θ is the fractional surface coverage and E_d is the desorption energy. The rate of desorption, $R_{des} = d\theta/dt$, was calculated as a function of temperature (T) over a TPD experiment such as that shown in Figure 2, and used to obtain the desorption energy based on eq. (II):[66-68]

$$R_{des} = -\frac{1}{\beta}\frac{d(\theta)}{dT} = -\frac{d(\theta)}{dt} = \nu(\theta,T)\frac{\theta}{(1-\theta)}\exp\left(-\frac{E_d(\theta)}{RT}\right) \qquad \text{(II)}$$

In eq. (II), β is the temperature ramp rate (0.25 K s^{-1}), $\nu(\theta,T)$ is the preexponential factor, $E_d(\theta)$ is the desorption energy, which is a function of surface coverage due to lateral interactions, R is the gas constant, and T is the absolute temperature. The surface coverage, θ, at each point during the TPD experiment can be found by numerical integration of the desorption rate curve.

From the relationship established in eq. (II), the desorption energy can be extracted from the experimental data using two complementary approaches. The first approach exploits the Arrhenius form of eq. (II), which allows it to be linearized in order to derive an estimate of E_d. Figure 3 shows typical plots of $\ln\left(\frac{R_{des}}{\theta/(1-\theta)}\right)$ as a function of 1/T, the slope of which yields the average coverage-independent desorption energy (E_d). Table 1 summarizes the values obtained using this approach across a number of experiments. The uncertainty-weighted average value of E_d from the Arrhenius analysis is 47.0 ± 8.2 kJ mol^{-1} (±1s), where s is the sample standard deviation of the average defined as $s = \sqrt{\sum\frac{(x_i - x_{sm})^2}{N-1}}$.

A second approach is to determine $E_d(\theta)$ using an inversion technique,[69] by rearranging eq. (II) to yield:

$$E_d(\theta) = -RTln\left(\frac{-d\theta/dt}{\nu\cdot\left(\frac{\square}{(1-\square)}\right)}\right) \qquad \text{(III)}$$

From eq. (III), $E_d(\theta)$ can be calculated from the measured values of $d\theta/dt$ for the highest initial coverage at an assumed value of ν. This value of $E_d(\theta)$ is then used to integrate eq. (II) and simulate the expected desorption curves at smaller surface coverages. Figure 4 shows the results of applying the inversion technique to the experimental data shown in Figure 2. The experimentally measured desorption rates at each coverage are compared to the simulated desorption rates (Fig. 4a) for each assumed value of ν, and the sum of the squared residuals between the two is calculated (Fig. 4b). The residuals are minimized by varying ν to obtain the best fit to the experimental data (Fig. 4a). The optimum value of ν is then used to determine $E_d(\theta)$ (Fig. 4c), the desorption energy as a function of surface coverage. Finally, the linear region of each $E_d(\theta)$ curve is extrapolated to zero coverage. Since the silica sample is not a single crystal, the surface structure is likely to be heterogeneous, leading to a distribution of binding site energies. The value of E_d obtained from linear extrapolation thus represents the desorption energy of an isolated molecule bound to the predominant type of surface site and not subject to lateral interactions. In addition, Table 1 summarizes the zero-coverage values obtained for E_d from inversion analysis of all the data sets reported in this work, with an uncertainty-weighted average value of 48.0 ± 3.4 kJ mol^{-1} (±1s).

Also shown in Table 1 are the best fit pre-exponential factors. It should be noted that these values of ν include the effects of desorption and readsorption of the limonene as it travels up through the silica particle multi-layers before desorbing into the vacuum, and are thus not true pre-exponential factors for the desorption of limonene from an unobstructed silica surface.[59, 70-75]

Nevertheless, the desorption energies derived using the inversion technique should not be affected by these processes.[73-75]

The coverage-independent values of E_d derived from both the Arrhenius analysis and the inversion method can be evaluated in light of previous results. In a series of papers[7, 53-56, 58] Grassian, Tobias and coworkers carried out experimental measurements of the adsorption and desorption kinetics of limonene from silica from 298–308 K using FTIR spectroscopy. Complementary molecular dynamics calculations and multiphase kinetic modeling[55] were used to calculate desorption energies in the range of 53–57 kJ mol^{-1} (uncertainties of ~ 8-9 kJ mol^{-1}), depending on the orientation of the limonene molecule on the SiO_2 surface. Additional calculations[56] based on the M06-2X density functional applied to the gas-phase and adsorbed limonene systems yielded desorption energies ranging from 41.6–46.3 kJ mol^{-1}, again depending on the surface orientation of the adsorbed limonene. Since the experimental technique in this work does not resolve differences in desorption energy due to molecular orientation, the mean E_d of 47.5 ± 8.2 kJ mol^{-1} presented here thus reflects an average value for the two orientations on the surface. While these results are, to the best of our knowledge, the first experimental measurements of the limonene-silica desorption energy over a broad temperature range, they are in good agreement with values calculated previously at higher temperatures.

Previous work has also attempted to better understanding the driving force behind the adsorption of the non-polar limonene molecule to the polar silica surface.[56] Silica surfaces have surface Si-OH and Si-O-Si bonds that can interact with incoming gases.[61] This presents the possibility of hydrogen bonding as well as London dispersion and dipole-induced dipole forces. *Ab initio* molecular dynamics calculations[7, 53-56, 58] and sum-frequency generation spectroscopy measurements[57] have shown that hydrogen bonding between the π-electrons in limonene and the surface Si-OH groups is a significant attractive force, along with dispersion forces. Interestingly, the double bond in the propenyl side group of limonene plays a major role in this hydrogen bonding, accounting for the orientational effect described previously: the most stable orientation for adsorbed limonene is that where the propenyl group is in closer contact with the surface.

Comparing these results with the desorption of benzene from silica further emphasizes the role which molecular structure plays in determining the desorption energetics of organic molecules. In previous TPD experiments,[59] the desorption energy for benzene on silica was measured as (34.5 ± 5.0) kJ mol^{-1} (±1σ), in excellent agreement with a value of (31.0 ± 2.3) kJ mol^{-1} (±1σ) reported earlier by Morris and coworkers[60] and in reasonable agreement with a calculated value of 28.3 kJ mol^{-1}.[56] This smaller surface binding energy of benzene is due in part to the weaker interaction between the aromatic π electrons and the silica Si-OH groups when compared with the π-hydrogen bonding interaction implicated in limonene adsorption. It should also be noted that values of E_d for limonene and benzene derived from these experiments and explicit calculations are smaller than those predicted by some parameterizations based on the molecular weight or polarizability of the adsorbate alone[76] Interestingly, that parameterization overestimates the magnitude of E_d, yielding 65 kJ mol^{-1} for limonene, and 47 kJ mol^{-1} for benzene, illustrating the importance of taking into account the molecular structures of both the gas and the surface to predict desorption energies.

Uptake Experiments: From the initial drop in signal on exposing the gas to the silica particles, the initial net uptake coefficient ($\gamma_{0,\mathrm{net}}$) can be obtained (eq. I). Initial net uptake coefficients were measured for limonene on silica at temperatures in 10 K intervals from 210–250 K, with typical uptake data at each temperature shown in Figure 5. There is initial rapid uptake until the signal reaches I_{min}, followed by a slower rate of uptake, corresponding to increased desorption as surface sites are filled. A constant signal (I_{ss}) is then reached. At this point, the signal has not returned to its initial value ($I_{ss} \neq I_o$), indicating steady-state conditions between uptake and desorption.

Figure 6 and Table 2 show values of $\gamma_{0,\mathrm{net}}$, which fall from $(1.7 \pm 0.3) \times 10^{-3}$ (±1s) to $(2.3 \pm 0.4) \times 10^{-4}$ (±1s) as temperature increases. By comparison, the value of the surface accommodation coefficient ($\alpha_{s,0}$) assumed in the kinetic model is 1, roughly three orders of magnitude larger. The output of the model suggests that the discrepancy between these values is primarily due to the desorption rate of limonene, which increases with temperature and is sufficiently fast to decrease the measured net uptake over this temperature range. An expression for absolute desorption rate constant employed in the model is given in Table S1.

The Langmuir model of adsorption predicts that surface coverage will depend on the gas pressure/concentration according to eq. (IV),

$$\frac{k_{ads}}{k_{des}}[G] = \frac{\theta}{(1-\theta)} \qquad \text{(IV)}$$

where [G] is the gas-phase concentration of the adsorbing molecule. Thus the ratio $k_{\mathrm{ads}}/k_{\mathrm{des}}$ can be obtained from a plot of $\theta/(1-\theta)$ against the gas-phase concentration at different temperatures, as described in the SI and shown in Figure S2a. A derivation of eq. (IV), as well as a description of how coverages were calculated for each uptake experiment, is given in the SI (Fig. S3). The resulting values of $k_{\mathrm{ads}}/k_{\mathrm{des}}$ are summarized in Table 2. Since adsorption is not expected to have an energy barrier, the temperature dependence of this ratio should primarily be controlled by the binding energy for the desorption step. Thus, an Arrhenius plot of $k_{\mathrm{ads}}/k_{\mathrm{des}}$ as a function of temperature would be expected to yield an activation energy of $-E_d$, after accounting for the expected square-root temperature dependence of $\mathrm{k}_{\mathrm{ads}}$ due to the temperature dependence of the gas collision frequency.

However, as seen in Figure S2b, the slope of the plot yields an activation energy of -23.7 kJ mol^{-1}, roughly half the magnitude of E_d determined from TPD experiments. Consistent with the kinetic modeling results discussed below, this is attributed to diffusion into the multilayers of silica particles, along with re-adsorption and desorption in the pores. As a result, the ratios $k_{\mathrm{ads}}/k_{\mathrm{des}}$ derived from Figure S2 are effective ratios, including desorption and re-adsorption effects, and not simply adsorption/desorption as for a true Langmuir equilibrium. Interestingly, despite the influence of diffusive limitations, extrapolation of these results to 298 K gives a value of the effective equilibrium constant that is in reasonable agreement with the value inferred by Fang et al.[55] for limonene adsorption on packed silica, as detailed in the SI (Fig. S4).

To provide further insight into the molecular processes which govern the net uptake, a kinetic multi-layer model was applied to the uptake profiles, as described previously.[59] Dashed red lines in Figure 5 show the fits to representative data using these parameters. Additional experimental runs and model fits across the 210–250 K temperature range can be found in the SI (Fig. S5–S17). It should again be noted that the surface accommodation coefficient (α_s) on an adsorbate free surface employed in the model is 1, reflecting efficient initial binding of the limonene to the surface. Figure 7 shows the model predicted concentrations of limonene adsorbed to the particle surfaces as well as the gas-phase concentrations in the pores at 210 K (Fig. 7a,b) and 250 K (Fig. 7c,d) as a function of time and distance from the top of the silica powder. Additional data for 230 and 240 K can be found in the SI (Fig. S18–S19). At 210 K, most of the adsorbed limonene is found in the top ~ 200 nm over the first minute of exposure (Fig. 7a) while at 250 K, it has penetrated throughout the silica (Fig. 7c) due to higher diffusion and desorption coefficients. The gas-phase concentrations in the pores mirror this behavior, with the highest concentrations near the surface at 210 K but rapidly distributing throughout the layers at 250 K (Fig. 7b,d). The effect of temperature on the distribution of limonene within the particle bed supports the idea that the derived values of $k_{\mathrm{ads}}/k_{\mathrm{des}}$ (Table 2, Fig. S2) do not solely reflect single adsorption and desorption processes from one surface site, but will rather be sensitive to the depth of the particle bed sampled by the uptake experiment.

Conclusions:

Quantifying the uptake and desorption of gases from surfaces has many important applications ranging from indoor and outdoor air pollution to the impact of such processes on materials and public health. This study reports fundamental data on the desorption energy and uptake of gaseous limonene on silica which are important compounds found in both indoor and outdoor environments. A relatively large binding energy of 47.5 kJ mol^{-1} reflects hydrogen bonding between the Si-OH surface groups and the double bonds of limonene, as postulated by others,[7, 54-57] and highlights the importance of the structure of both the gas and the surface in determining the energetics of desorption. The uptake kinetics are shown to be consistent with a surface accommodation coefficient of one, with rapid desorption playing an important role in lowering the measured initial uptake coefficient by several orders of magnitude. The fundamental interactions between limonene and silica involve hydrogen bonding between the Si-OH groups and the double bonds in limonene, so the values measured here should hold regardless of differences in the morphology of the silica surface.

In addition to reporting on fundamental physical parameters of adsorbed organic molecules, the combined experimental/modeling approach demonstrated here can provide much-needed insight into how gases interact with porous surfaces. Building materials such as concrete, drywall, paint etc. are porous[77-80] and take up gases from various activities including cooking and cleaning indoors[81-83] and exposure to both anthropogenic and biogenic species outdoors.[11] In addition, wildfire emissions have been shown to impact both the exteriors and interiors of buildings,[84] causing the issue of gas uptake on and subsequent degassing from building materials to take on new public health implications. Measurements of desorption kinetics from porous materials are crucial in developing our understanding of these important everyday processes.

Acknowledgements:

We are very grateful to the National Science Foundation (AGS-2030175, AGS-2246502) and our Program Officer Sylvia Edgerton for support of this work. We thank Mark Steinborn, Shane Embleton and Dustin Cedarholm for machining assistance, Maik Bollhorn for glassblowing, and Doug Tobias for helpful discussions.

Supplementary Information: Experimental schematic, Figure S1; Kinetic Model Description and Table of Parameters, Table S1; Figure S2, Effective Langmuir coefficients; Derivation of eqn. (IV) from main text; Derivation of fractional coverage (θ) from uptake profiles, Figure S3; Comparison of Effective Langmuir Coefficients (k_{ads}/k_{des}) from uptake experiments, Figure S4; Additional uptake experiments and model output, Figures S5–S17, Uptake experiments and model outputs 210 – 250 K; Figure S18–S19, Adsorbed limonene and porous gas-phase limonene concentration profiles from the model at 210, 230, 240, and 250 K.

Table 1. Summary of desorption energies for limonene on silica particles using two different analytical approaches.

Substrate (# curves)[a]	**Average E_d (± 1s)[d] (kJ mol^{-1})[b]**	**E_d as $\theta \rightarrow 0$ (± 2s) (kJ mol^{-1})[c]**	**ν (s^{-1})**
Silicon wafer (4)	50.1 ± 2.6	47.7 ± 0.1	7.5
Silicon wafer (2)	45.8 ± 0.9	49.0 ± 0.1	7.0
Silicon wafer (3)	48.7 ± 1.0	48.7 ± 0.2	7.5
Copper (2)	45.5 ± 2.1	44.6 ± 0.2	7.0
Copper (4)	37.8 ± 5.9	47.6 ± 0.3	7.5
AVERAGE[e] ±1s	47.0 ± 8.2	48.0 ± 3.4	7.3 ± 0.3

[a] Number of TPD sub-monolayer curves in experiment.

[b] From the slope of plots of $\ln(R_{des}/(\theta/(1-\theta)))$ vs. T^{-1}.

[c] From inversion analysis extrapolated to zero surface coverage.

[d] Defined as $s = \sqrt{\sum \frac{(x_i - x_{sm})^2}{N-1}}$ where x_i are the sample values, x_{sm} is the sample mean and N is the number of data points. Uncertainties do not explicitly account for uncertainty in the estimation of the area of a monolayer coverage.

[e] Average of experimental values weighted by uncertainty ($1/s^2$).

Table 2. Summary of initial uptake coefficients and the effective ratios k_{ads}/k_{des} for limonene on silica particles.

T (K)	**γ_0 (±1s)**	**$(k_{ads}/k_{des})^{eff}$ (cm^3 molecule^{-1})[a]**

210	$(1.7 \pm 0.3) \times 10^{-3}$	1.8×10^{-13}
220	$(9.5 \pm 5.7) \times 10^{-4}$	1.1×10^{-13}
230	$(6.2 \pm 0.5) \times 10^{-4}$	6.1×10^{-14}
240	$(2.9 \pm 0.6) \times 10^{-4}$	2.5×10^{-14}
250	$(2.3 \pm 0.4) \times 10^{-4}$	2.8×10^{-14}

[a] See text for description of why these are effective ratios.

Figure Captions

Figure 1. Schematic of processes involved in gas uptake and desorption of limonene onto the agglomerated chain-like structures of fumed silica.

Figure 2. Typical TPD data for desorption of limonene from silica particles at different extents of surface coverage (θ). The blue trace illustrates a bimodal distribution due to desorption from both a multilayer and monolayer. The dashed gold trace is obtained by deconvolution of the blue trace and is taken as the monolayer, $\theta_0 = 1$. The remaining traces, resulting from higher annealing temperatures, illustrate successively smaller initial coverages.

Figure 3. Typical plot of $\ln [R_{des} / (\theta/(1-\theta))]$ as a function of T^{-1} for the experiment shown in Figure 2. The solid line represents a fit to the linear region of the curve corresponding to the largest initial sub-monolayer coverage; the dashed line represents a fit to the smallest initial coverage. (Units of R_{des} are ml. s^{-1}, or monolayers per second.)

Figure 4. Inversion analysis of TPD data shown in Fig. 2. (a) predicted TPD curves (lines) compared to the data in Fig. 2; (b) residuals for the inversion analysis; (c) desorption energy as a function of $\theta/(1-\theta)$.

Figure 5. Typical uptake profiles for limonene on silica particles at representative temperatures from 210–250 K. Kinetic multilayer model results are shown by the dashed red lines.

Figure 6. Temperature dependence of the initial net uptake coefficient. Error bars represent ±1s.

Figure 7. Kinetic multilayer model predictions of concentrations of limonene in the gas phase and on the silica particle surfaces, as a function of time and depth into the particle bed. (a, c) adsorbed limonene (molecule cm^{-2}) at 210 and 250 K; (b, d) gas-phase limonene in pores at 210 and 250 K respectively. Pressures indicate limonene gas pressure prior to opening sample lid. (Note the difference in vertical axis scale between top and bottom rows.)

References

1. H. Akimoto and J. Hirokawa, *Atmospheric Multiphase Chemistry*, Wiley, Hoboken, N.J., 2020.
2. A. P. Ault, V. H. Grassian, N. Carslaw, D. B. Collins, H. Destaillats, D. J. Donaldson, D. K. Farmer, J. L. Jimenez, V. F. McNeill, G. C. Morrison, R. E. O'Brien, M. Shiraiwa, M. E. Vance, J. R. Wells and W. Xiong, Indoor Surface Chemistry: Developing a Molecular Picture of Reactions on Indoor Interfaces, *Chem*, 2020, **6**, 3203-3218.
3. R. C. Chapleski, Y. F. Zhang, D. Troya and J. R. Morris, Heterogeneous chemistry and reaction dynamics of the atmospheric oxidants, O_3, NO_3, and OH, on organic surfaces, *Chem. Soc. Rev.*, 2016, **45**, 3731-3746.
4. B. J. Finlayson-Pitts and J. N. Pitts, *Chemistry of the Upper and Lower Atmosphere: Theory, Experiments, and Applications*, Academic Press, 2000.
5. S. Gligorovski and J. P. D. Abbatt, An indoor chemical cocktail, *Science*, 2018, **359**, 632-633.
6. Y. Liu, A. G. Bé, V. W. Or, M. R. Alves, V. H. Grassian and F. M. Geiger, Challenges and Opportunities in Molecular-Level Indoor Surface Chemistry and Physics, *Cell Rep. Phys. Sci.*, 2020, **1**.
7. M. von Domaros and D. J. Tobias, Molecular Dynamics Simulations of the Interactions of Organic Compounds at Indoor Relevant Surfaces, *Annu. Rev. Phys. Chem.*, 2025, DOI: 10.1146/annurev-physchem-083122-123017, 1-22.
8. M. L. Diamond, S. E. Gingrich, K. Fertuck, B. E. McCarry, G. A. Stern, B. Billeck, B. Grift, D. Brooker and T. D. Yager, Evidence for organic film on an impervious urban surface: characterization and potential teratogenic effects, *Environ. Sci. Technol.*, 2000, **34**, 2900-2908.
9. E. M. Hodge, M. L. Diamond, B. E. McCarry, G. A. Stern and P. A. Harper, Sticky windows: chemical and biological characteristics of the organic film derived from particulate and gas-phase air contaminants found on an urban impervious surface, *Arch. Environ. Con. Tox.*, 2003, **44**, 421-429.
10. B. Lam, M. L. Diamond, A. J. Simpson, P. A. Makar, J. Truong and N. A. Hernandez-Martinez, Chemical composition of surface films on glass windows and implications for atmospheric chemistry, *Atmos. Environ.*, 2005, **39**, 6578-6586.
11. D. J. Donaldson, A Brief History of (Urban) Grime, *ACS Earth Space Chem.*, 2025, **9**, 201-206.
12. W. W. Nazaroff and C. J. Weschler, Cleaning products and air fresheners: exposure to primary and secondary air pollutants, *Atmos. Environ.*, 2004, **38**, 2841-2865.

13. N. E. Klepeis, W. C. Nelson, W. R. Ott, J. P. Robinson, A. M. Tsang, P. Switzer, J. V. Behar, S. C. Hern and W. H. Engelmann, The National Human Activity Pattern Survey (NHAPS): a resource for assessing exposure to environmental pollutants, *J. Exposure Anal. Environ. Epidemiol.*, 2001, **11**, 231-252.
14. L. Morawska, J. Allen, W. Bahnfleth, B. Bennett, P. M. Bluyssen, A. Boerstra, G. Buonanno, J. Cao, S. J. Dancer, A. Floto, F. Franchimon, T. Greenhalgh, C. Haworth, J. Hogeling, C. Isaxon, J. L. Jimenez, A. Kennedy, P. Kumar, J. Kurnitski, Y. Li, M. Loomans, G. Marks, L. C. Marr, L. Mazzarella, A. K. Melikov, S. L. Miller, D. K. Milton, J. Monty, P. V. Nielsen, C. Noakes, J. Peccia, K. A. Prather, X. Querol, T. Salthammer, C. Sekhar, O. Seppanen, S. I. Tanabe, J. W. Tang, R. Tellier, K. W. Tham, P. Wargocki, A. Wierzbicka and M. Yao, Mandating indoor air quality for public buildings, *Science*, 2024, **383**, 1418-1420.
15. W. C. Hinds, *Aerosol Technology: Properties, Behavior, and Measurement of Airborne Particles*, John Wiley & Sons, 1982.
16. M. Kanakidou, J. H. Seinfeld, S. N. Pandis, I. Barnes, F. J. Dentener, M. C. Facchini, R. Van Dingenen, B. Ervens, A. Nenes, C. J. Nielsen, E. Swietlicki, J. P. Putaud, Y. Balkanski, S. Fuzzi, J. Horth, G. K. Moortgat, R. Winterhalter, C. E. L. Myhre, K. Tsigaridis, E. Vignati, E. G. Stephanou and J. Wilson, Organic aerosol and global climate modelling: a review, *Atmos. Chem. Phys.*, 2005, **5**, 1053-1123.
17. A. Singh, W. J. Bloss and F. D. Pope, 60 years of UK visibility measurements: impact of meteorology and atmospheric pollutants on visibility, *Atmos. Chem. Phys.*, 2017, **17**, 2085-2101.
18. D. K. Farmer, C. D. Cappa and S. M. Kreidenweis, Atmospheric processes and their controlling influence on cloud condensation nuclei activity, *Chem. Rev.*, 2015, **115**, 4199-4217.
19. E. A. Fofie, N. M. Donahue and A. Asa-Awuku, Cloud condensation nuclei activity and droplet formation of primary and secondary organic aerosol mixtures, *Aerosol Sci. Technol.*, 2017, **52**, 242-251.
20. V. F. McNeill, Atmospheric Aerosols: Clouds, Chemistry, and Climate, *Annu. Rev. Chem. Biomol. Eng.*, 2017, **8**, 427-444.
21. J. Schmale, S. Henning, S. Decesari, B. Henzing, H. Keskinen, K. Sellegri, J. Ovadnevaite, M. L. Pöhlker, J. Brito, A. Bougiatioti, A. Kristensson, N. Kalivitis, I. Stavroulas, S. Carbone, A. Jefferson, M. Park, P. Schlag, Y. Iwamoto, P. Aalto, M. Äijälä, N. Bukowiecki, M. Ehn, G. Frank, R. Fröhlich, A. Frumau, E. Herrmann, H. Herrmann, R. Holzinger, G. Kos, M. Kulmala, N. Mihalopoulos, A. Nenes, C. O'Dowd, T. Petäjä, D. Picard, C. Pöhlker, U. Pöschl, L. Poulain, A. S. H. Prévôt, E. Swietlicki, M. O. Andreae, P. Artaxo, A. Wiedensohler, J. Ogren, A. Matsuki, S. S. Yum, F. Stratmann, U. Baltensperger and M. Gysel, Long-term cloud condensation nuclei number concentration, particle number size distribution and chemical composition measurements at regionally representative observatories, *Atmos. Chem. Phys.*, 2018, **18**, 2853-2881.
22. S. Twomey, Aerosols, clouds and radiation, *Atmos. Environ.*, 1991, **25A**, 2435-2442.
23. R. F. Phalen, *Inhalation studies: Foundation and techniques*, Informa Healthcare, 2009.
24. P. J. Landrigan, R. Fuller, H. Hu, J. Caravanos, M. L. Cropper, D. Hanrahan, K. Sandilya, T. C. Chiles, P. Kumar and W. A. Suk, Pollution and Global Health - An Agenda for Prevention, *Environ. Health Perspect.*, 2018, **126**, 084501.

25. J. Lelieveld, J. S. Evans, M. Fnais, D. Giannadaki and A. Pozzer, The contribution of outdoor air pollution sources to premature mortality on a global scale, *Nature*, 2015, **525**, 367-371.
26. C. A. Pope, 3rd and D. W. Dockery, Health effects of fine particulate air pollution: lines that connect, *J. Air Waste Manage. Assoc.*, 2006, **56**, 709-742.
27. U. Pöschl and M. Shiraiwa, Multiphase Chemistry at the Atmosphere–Biosphere Interface Influencing Climate and Public Health in the Anthropocene, *Chem. Rev.*, 2015, **115**, 4440-4475.
28. R. Fuller, P. J. Landrigan, K. Balakrishnan, G. Bathan, S. Bose-O'Reilly, M. Brauer, J. Caravanos, T. Chiles, A. Cohen, L. Corra, M. Cropper, G. Ferraro, J. Hanna, D. Hanrahan, H. Hu, D. Hunter, G. Janata, R. Kupka, B. Lanphear, M. Lichtveld, K. Martin, A. Mustapha, E. Sanchez-Triana, K. Sandilya, L. Schaefli, J. Shaw, J. Seddon, W. Suk, M. M. Tellez-Rojo and C. Yan, Pollution and health: a progress update, *Lancet Planet Health*, 2022, **6**, e535-e547.
29. M. R. Heal, P. Kumar and R. M. Harrison, Particles, air quality, policy and health, *Chem. Soc. Rev.*, 2012, **41**, 6606-6630.
30. J. E. Thompson, Airborne Particulate Matter: Human Exposure and Health Effects, *J. Occup. Environ. Med.*, 2018, **60**, 392-423.
31. H. O. T. Pye, C. K. Ward-Caviness, B. N. Murphy, K. W. Appel and K. M. Seltzer, Secondary organic aerosol association with cardiorespiratory disease mortality in the United States, *Nat. Commun.*, 2021, **12**, 7215.
32. S. Rajagopalan, R. D. Brook, P. Salerno, B. Bourges-Sevenier, P. Landrigan, M. J. Nieuwenhuijsen, T. Munzel, S. V. Deo and S. Al-Kindi, Air pollution exposure and cardiometabolic risk, *Lancet Diabetes Endocrinol.*, 2024, **12**, 196-208.
33. S. J. Segalowitz, Public health, brain health, and the dangers of air pollution for neural development, *Brain and Cognition*, 2008, **68**, 115-116.
34. N. C. Alter, E. M. Whitman, D. C. Bellinger and P. J. Landrigan, Quantifying the association between PM(2.5) air pollution and IQ loss in children: a systematic review and meta-analysis, *Environ. Health*, 2024, **23**, 101.
35. A. Peters, R. Ruckerl and J. Cyrys, Lessons from air pollution epidemiology for studies of engineered nanomaterials, *J. Occup. Environ. Med.*, 2011, **53**, S8-S13.
36. A. Peters, B. Veronesi, L. Calderon-Garciduenas, P. Gehr, L. C. Chen, M. Geiser, W. Reed, B. Rothen-Rutishauser, S. Schurch and H. Schulz, Translocation and potential neurological effects of fine and ultrafine particles a critical update, *Part. Fibre Toxicol.*, 2006, **3**, 13.
37. D. T. Limmer, A. W. Gotz, T. H. Bertram and G. M. Nathanson, Molecular Insights into Chemical Reactions at Aqueous Aerosol Interfaces, *Annu. Rev. Phys. Chem.*, 2024, **75**, 111-135.
38. M. Shiraiwa, R. M. Garland and U. Pöschl, Kinetic double-layer model of aerosol surface chemistry and gas-particle interactions (K2-SURF): Degradation of polycyclic aromatic hydrocarbons exposed to O_3, NO_2, H_2O, OH and NO_3, *Atmos. Chem. Phys.*, 2009, **9**, 9571-9586.
39. M. Shiraiwa and U. Pöschl, Mass accommodation and gas–particle partitioning in secondary organic aerosols: dependence on diffusivity, volatility, particle-phase reactions, and penetration depth, *Atmos. Chem. Phys.*, 2021, **21**, 1565-1580.

40. T. Koop, J. Bookhold, M. Shiraiwa and U. Poschl, Glass transition and phase state of organic compounds: dependency on molecular properties and implications for secondary organic aerosols in the atmosphere, *Phys. Chem. Chem. Phys.*, 2011, **13**, 19238-19255.
41. A. C. Vander Wall, V. Perraud, L. M. Wingen and B. J. Finlayson-Pitts, Evidence for a kinetically controlled burying mechanism for growth of high viscosity secondary organic aerosol, *Environ. Sci.: Processes Impacts*, 2020, **22**, 66-83.
42. A. C. Vander Wall, L. M. Wingen, V. Perraud, Y. Zhao and B. J. Finlayson-Pitts, Enhanced Gas Uptake during α-Pinene Ozonolysis Points to a Burying Mechanism, *ACS Earth Space Chem.*, 2020, **4**, 1435-1447.
43. S. Gu, W. Luo, A. Charmchi, K. J. McWhirter, T. Rosenstiel, J. Pankow and C. L. Faiola, Limonene Enantiomeric Ratios from Anthropogenic and Biogenic Emission Sources, *Environ. Sci. Technol. Lett.*, 2024, **11**, 130-135.
44. N. Carslaw and D. Shaw, Modification of cleaning product formulations could improve indoor air quality, *Indoor Air*, 2022, **32**, e13021.
45. C. Ravichandran, P. C. Badgujar, P. Gundev and A. Upadhyay, Review of toxicological assessment of *d*-limonene, a food and cosmetics additive, *Food Chem. Toxicol.*, 2018, **120**, 668-680.
46. E. Uhde and N. Schulz, Impact of room fragrance products on indoor air quality, *Atmos. Environ.*, 2015, **106**, 492-502.
47. R. Sheu, C. F. Fortenberry, M. J. Walker, A. Eftekhari, C. Stonner, A. Bakker, J. Peccia, J. Williams, G. C. Morrison, B. J. Williams and D. R. Gentner, Evaluating Indoor Air Chemical Diversity, Indoor-to-Outdoor Emissions, and Surface Reservoirs Using High-Resolution Mass Spectrometry, *Environ. Sci. Technol.*, 2021, **55**, 10255-10267.
48. M. R. Lederer, A. R. Staniec, Z. L. Coates Fuentes, D. A. Van Ry and R. Z. Hinrichs, Heterogeneous Reactions of Limonene on Mineral Dust: Impacts of Adsorbed Water and Nitric Acid, *J. Phys. Chem. A*, 2016, **120**, 9545-9556.
49. C. J. Weschler and H. C. Shields, Indoor ozone/terpene reactions as a source of indoor particles, *Atmos. Environ.*, 1999, **33**, 2301-2312.
50. M. S. Waring and J. A. Siegel, Indoor secondary organic aerosol formation initiated from reactions between ozone and surface-sorbed D-limonene, *Environ. Sci. Technol.*, 2013, **47**, 6341-6348.
51. F. Jacob, N. Houzel, P. Genevray, C. Clety, C. Coeur, E. Perdrix, L. Y. Alleman, S. Anthérieu, G. Garçon, G. Dhont, A. Cuisset, J. M. Lo Guidice and A. Tomas, New insights into the chemical composition and formation mechanisms of secondary organic aerosols produced in the ozonolysis of limonene, *J. Aerosol Sci.*, 2023, **173**.
52. V. W. Or, M. Wade, S. Patel, M. R. Alves, D. Kim, S. Schwab, H. Przelomski, R. O'Brien, D. Rim, R. L. Corsi, M. E. Vance, D. K. Farmer and V. H. Grassian, Glass surface evolution following gas adsorption and particle deposition from indoor cooking events as probed by microspectroscopic analysis, *Environ. Sci.: Processes Impacts*, 2020, **22**, 1698-1709.
53. H. Fan, P. S. J. Lakey, E. S. Frank, D. J. Tobias, M. Shiraiwa and V. H. Grassian, Comparison of the Adsorption–Desorption Kinetics of Limonene and Carvone on TiO_2 and SiO_2 Surfaces under Different Relative Humidity Conditions, *J. Phys. Chem. C*, 2022, **126**, 21253-21262.

54. L. Huang, E. S. Frank, S. Riahi, D. J. Tobias and V. H. Grassian, Adsorption of constitutional isomers of cyclic monoterpenes on hydroxylated silica surfaces, *J. Chem. Phys.*, 2021, **154**, 124703.
55. Y. Fang, P. S. J. Lakey, S. Riahi, A. T. McDonald, M. Shrestha, D. J. Tobias, M. Shiraiwa and V. H. Grassian, A molecular picture of surface interactions of organic compounds on prevalent indoor surfaces: limonene adsorption on SiO_2, *Chem. Sci.*, 2019, **10**, 2906-2914.
56. Y. Fang, S. Riahi, A. T. McDonald, M. Shrestha, D. J. Tobias and V. H. Grassian, What Is the Driving Force behind the Adsorption of Hydrophobic Molecules on Hydrophilic Surfaces?, *J. Phys. Chem. Lett.*, 2019, **10**, 468-473.
57. Y. Liu, H. M. Chase and F. M. Geiger, Partially (*resp*. fully) reversible adsorption of monoterpenes (*resp*. alkanes and cycloalkanes) to fused silica, *J. Chem. Phys.*, 2019, **150**, 074701.
58. E. S. Frank, H. Fan, M. Shrestha, S. Riahi, D. J. Tobias and V. H. Grassian, Impact of Adsorbed Water on the Interaction of Limonene with Hydroxylated SiO_2: Implications of π-Hydrogen Bonding for Surfaces in Humid Environments, *J. Phys. Chem. A*, 2020, **124**, 10592-10599.
59. K. N. Johnson, Y. Li, M. J. Ezell, P. S. J. Lakey, M. Shiraiwa and B. J. Finlayson-Pitts, Elucidating gas-surface interactions relevant to atmospheric particle growth using combined temperature programmed desorption and temperature-dependent uptake, *Phys. Chem. Chem. Phys.*, 2024, **26**, 23264-23276.
60. J. Abelard, A. R. Wilmsmeyer, A. C. Edwards, W. O. Gordon, E. M. Durke, C. J. Karwacki, D. Troya and J. R. Morris, Adsorption of Substituted Benzene Derivatives on Silica: Effects of Electron Withdrawing and Donating Groups, *J. Phys. Chem. C*, 2016, **120**, 13024-13031.
61. A. V. Kiselev and V. I. Lygin, *Infrared Spectra of Surface Compounds*, John Wiley & Sons, New York, 1975.
62. in *NIST Chemistry WebBook, NIST Standard Reference Database Number 69*, eds. P. J. Linstrom and W. G. Mallard, National Institute of Standards and Technology, Gaithersburg MD, 20899, DOI: 10.18434/T4D303, ch. Mass Spectra.
63. P. S. J. Lakey, G. C. Morrison, Y. Won, K. M. Parry, M. von Domaros, D. J. Tobias, D. Rim and M. Shiraiwa, The impact of clothing on ozone and squalene ozonolysis products in indoor environments, *Commun. Chem.*, 2019, **2**, 1-8.
64. H. Fan, E. S. Frank, P. S. J. Lakey, M. Shiraiwa, D. J. Tobias and V. H. Grassian, Heterogeneous Interactions between Carvone and Hydroxylated SiO_2, *J. Phys. Chem. C*, 2022, **126**, 6267-6279.
65. M. von Domaros, P. S. J. Lakey, M. Shiraiwa and D. J. Tobias, Multiscale Modeling of Human Skin Oil-Induced Indoor Air Chemistry: Combining Kinetic Models and Molecular Dynamics, *J. Phys. Chem. B*, 2020, **124**, 3836-3843.
66. C. T. Campbell, L. H. Sprowl and L. Árnadóttir, Equilibrium Constants and Rate Constants for Adsorbates: Two-Dimensional (2D) Ideal Gas, 2D Ideal Lattice Gas, and Ideal Hindered Translator Models, *J. Phys. Chem. C*, 2016, **120**, 10283-10297.
67. R. I. Masel, *Principles of Adsorption and Reaction on Solid Surfaces*, John Wiley & Sons, New York, 1996.
68. P. A. Redhead, Thermal desorption of gases, *Vacuum*, 1962, **12**, 203-211.

69. R. S. Smith and B. D. Kay, Desorption Kinetics of Benzene and Cyclohexane from a Graphene Surface, *J. Phys. Chem. B*, 2018, **122**, 587-594.

70. D. D. Beck, J. M. White and C. T. Ratcliffe, Catalytic Reduction of CO with Hydrogen-Sulfide. 2. Adsorption of H_2O And H_2S on Anatase and Rutile, *J. Phys. Chem.*, 1986, **90**, 3123-3131.

71. R. J. Cvetanović and Y. Amenomiya, A Temperature Programmed Desorption Technique for Investigation of Practical Catalysts, *Catal. Rev.*, 1972, **6**, 21-48.

72. J. L. Falconer and J. A. Schwarz, Temperature-Programmed Desorption and Reaction: Applications to Supported Catalysts, *Catal. Rev.: Sci. Eng.*, 1983, **25**, 141-227.

73. R. J. Gorte, Design parameters for temperature programmed desorption from porous catalysts, *J. Catal.*, 1982, **75**, 164-174.

74. M. B. Hugenschmidt, L. Gamble and C. T. Campbell, The interaction of H_2O with a TiO_2(110) surface, *Surf. Sci.*, 1994, **302**, 329-340.

75. A. R. Wilmsmeyer, J. Uzarski, P. J. Barrie and J. R. Morris, Interactions and binding energies of dimethyl methylphosphonate and dimethyl chlorophosphate with amorphous silica, *Langmuir*, 2012, **28**, 10962-10967.

76. D. A. Knopf, M. Ammann, T. Berkemeier, U. Pöschl and M. Shiraiwa, Desorption lifetimes and activation energies influencing gas–surface interactions and multiphase chemical kinetics, *Atmos. Chem. Phys.*, 2024, **24**, 3445-3528.

77. J. P. Downey, P. S. J. Lakey, M. Shiraiwa and J. P. D. Abbatt, Ozone Loss on Painted Surfaces: Dependence on Relative Humidity, Aging, and Exposure to Reactive SVOCs, *Environ. Sci. Technol.*, 2024, **58**, 12073-12081.

78. L. B. Algrim, D. Pagonis, J. A. de Gouw, J. L. Jimenez and P. J. Ziemann, Measurements and modeling of absorptive partitioning of volatile organic compounds to painted surfaces, *Indoor Air*, 2020, **30**, 745-756.

79. R. Meininghaus and E. Uhde, Diffusion studies of VOC mixtures in a building material, *Indoor Air*, 2002, **12**, 215-222.

80. P. Blondeau, A. L. Tiffonnet, F. Allard and F. Haghighat, Physically Based Modelling of the Material and Gaseous Contaminant Interactions in Buildings: Models, Experimental Data and Future Developments, *Adv. Build. Energy. Res.*, 2008, **2**, 57-93.

81. R. Habre, D. C. Dorman, J. Abbatt, W. P. Bahnfleth, E. Carter, D. Farmer, G. Gawne-Mittelstaedt, A. H. Goldstein, V. H. Grassian, G. Morrison, J. Peccia, D. Poppendieck, K. A. Prather, M. Shiraiwa, H. M. Stapleton, M. Williams and M. E. Harries, Why Indoor Chemistry Matters: A National Academies Consensus Report, *Environ. Sci. Technol.*, 2022, **56**, 10560-10563.

82. C. G. Masoud, Y. Li, D. S. Wang, E. F. Katz, P. F. DeCarlo, D. K. Farmer, M. E. Vance, M. Shiraiwa and L. Hildebrandt Ruiz, Molecular composition and gas-particle partitioning of indoor cooking aerosol: Insights from a FIGAERO-CIMS and kinetic aerosol modeling, *Aerosol Sci. Technol.*, 2022, **56**, 1156-1173.

83. R. E. O'Brien, Y. Li, K. J. Kiland, E. F. Katz, V. W. Or, E. Legaard, E. Q. Walhout, C. Thrasher, V. H. Grassian, P. F. DeCarlo, A. K. Bertram and M. Shiraiwa, Emerging investigator series: chemical and physical properties of organic mixtures on indoor surfaces during HOMEChem, *Environ. Sci.: Processes Impacts*, 2021, **23**, 559-568.

84. W. D. Dresser, J. M. Silberstein, C. E. Reid, M. E. Vance, C. Wiedinmyer, M. P. Hannigan and J. A. de Gouw, Volatile Organic Compounds Inside Homes Impacted by Smoke from the Marshall Fire, *ACS EST Air*, 2025, **2**, 4-12.

Data Availability Statement:

All data are shown in the paper or the SI.

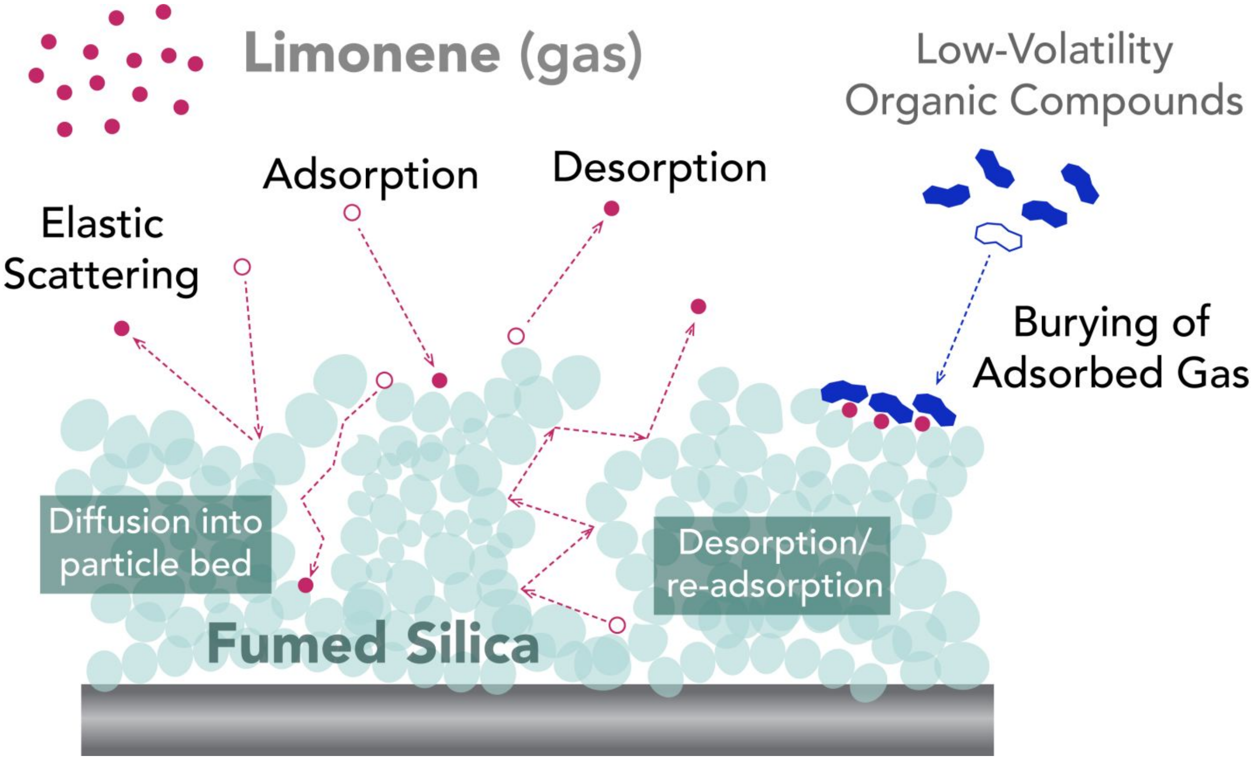

Figure 1. Schematic of processes involved in gas uptake and desorption of limonene onto the agglomerated chain-like structures of fumed silica.

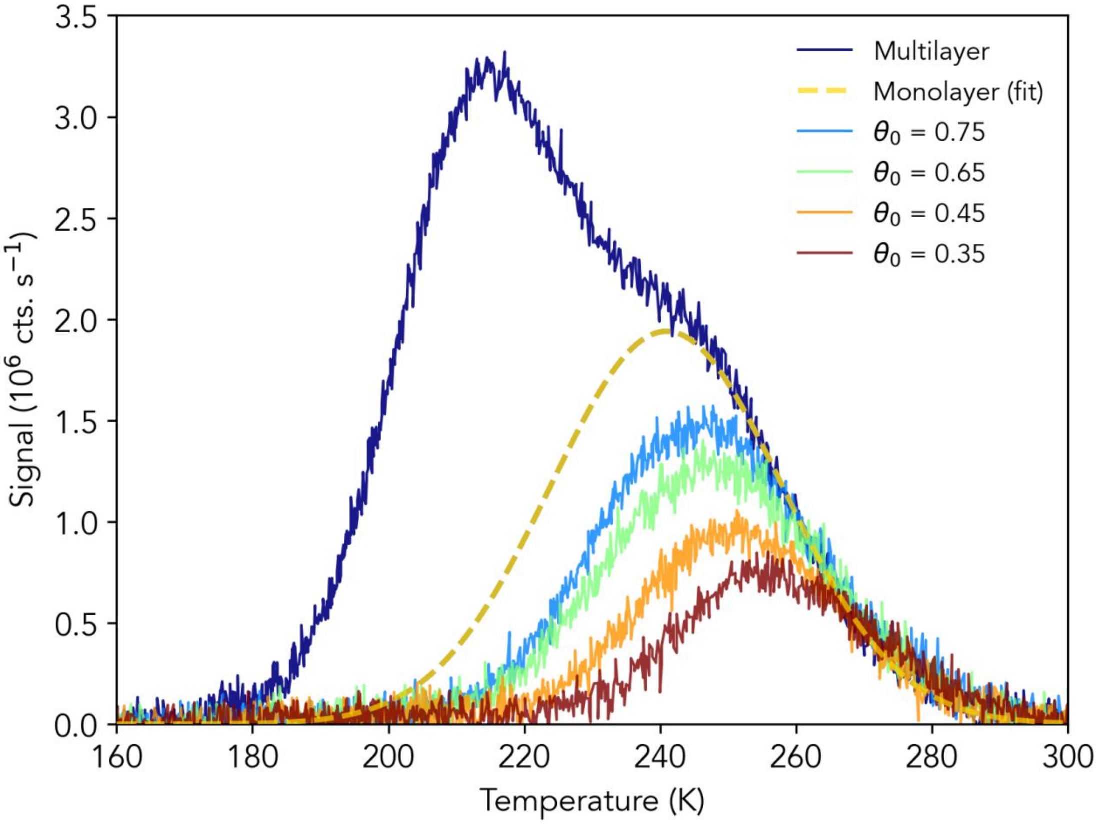

Figure 2. Typical TPD data for desorption of limonene from silica particles at different extents of surface coverage (θ). The blue trace illustrates a bimodal distribution due to desorption from both a multilayer and monolayer. The dashed gold trace is obtained by deconvolution of the blue trace and is taken as the monolayer, $\theta_0 = 1$. The remaining traces, resulting from higher annealing temperatures, illustrate successively smaller initial coverages.

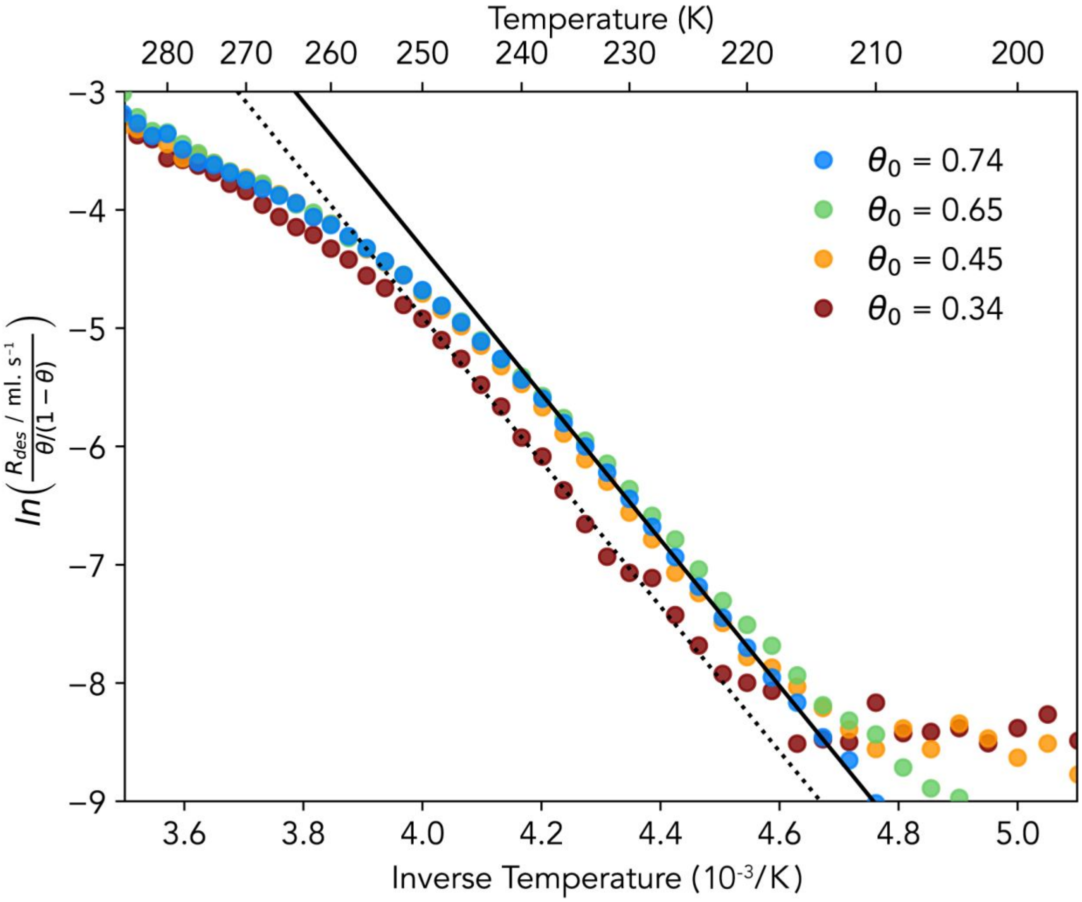

Figure 3. Typical plot of ln [R_{des} / (θ/(1-θ))] as a function of T^{-1} for the experiment shown in Figure 2. The solid line represents a fit to the linear region of the curve corresponding to the largest initial sub-monolayer coverage; the dashed line represents a fit to the smallest initial coverage. (Units of R_{des} are ml. s^{-1}, or monolayers per second.)

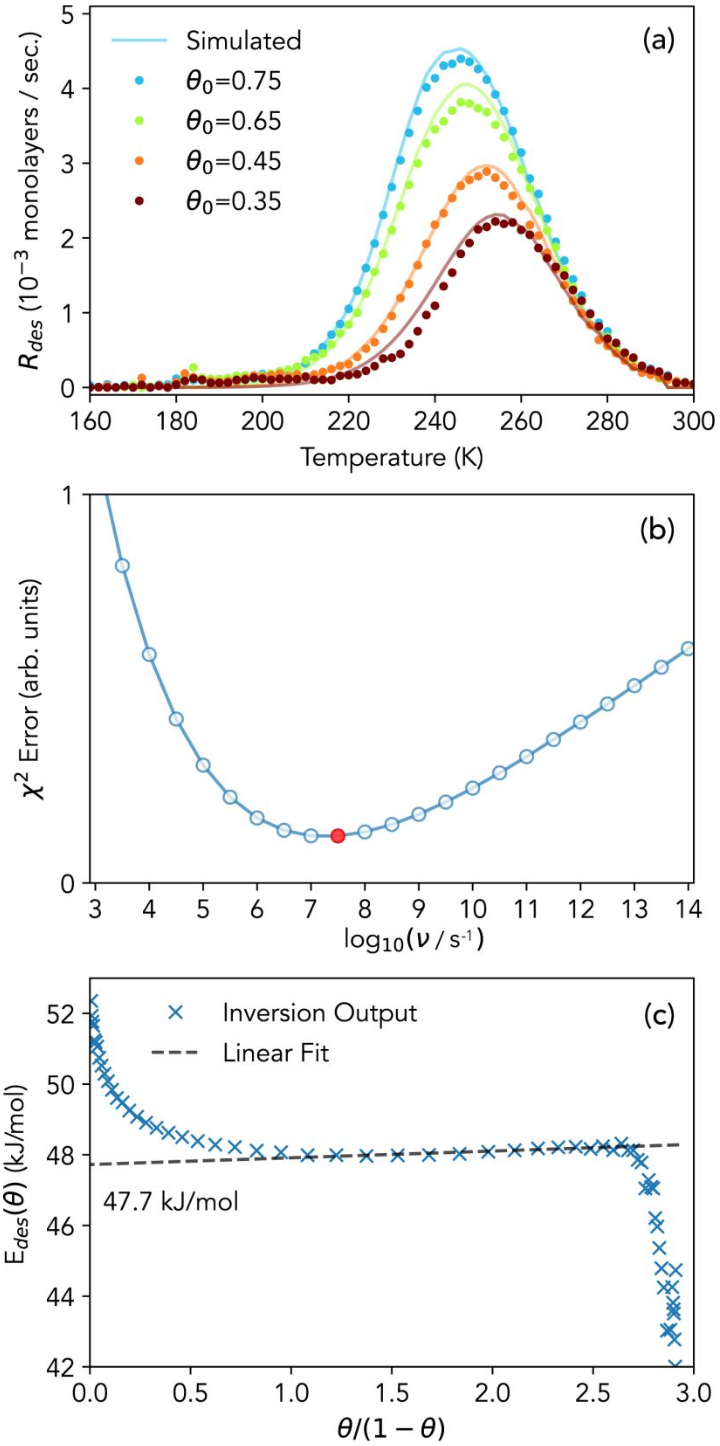

Figure 4. Inversion analysis of TPD data shown in Figure 2. (a) predicted TPD curves (lines) compared to the data in Figure 1; (b) residuals for the inversion analysis; (c) desorption energy as a function of θ/(1-θ).

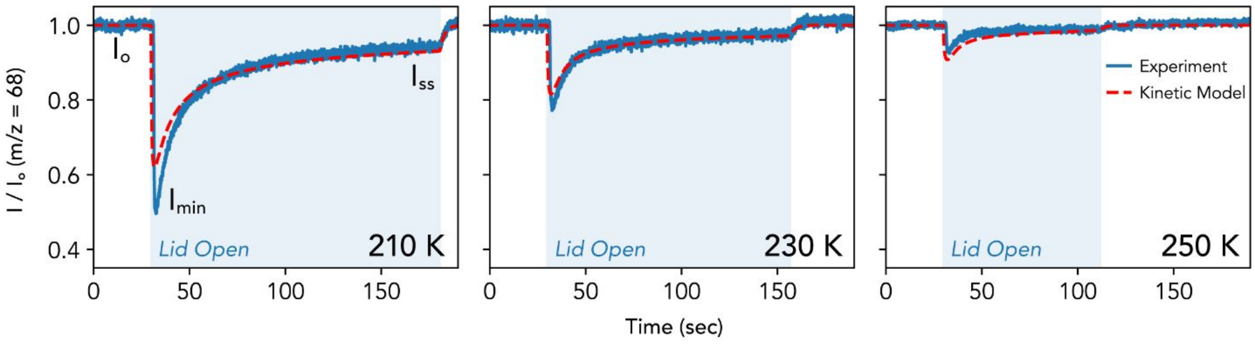

Figure 5. Typical uptake profiles for limonene on silica particles at representative temperatures from 210–250 K. Kinetic multilayer model results are shown by the dashed red lines.

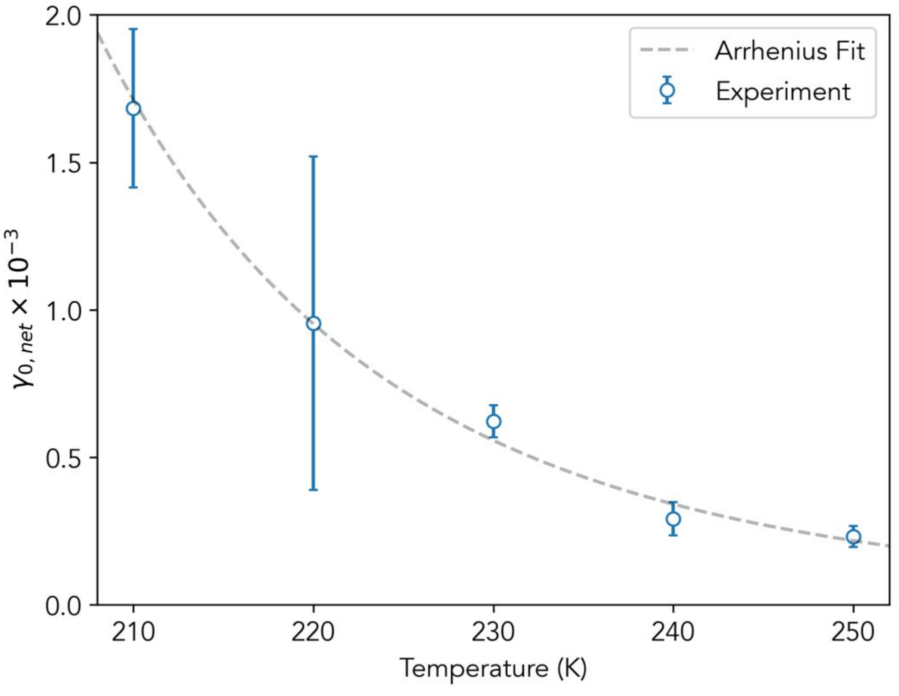

Figure 6. Temperature dependence of the initial net uptake coefficient. Error bars represent ±1s.

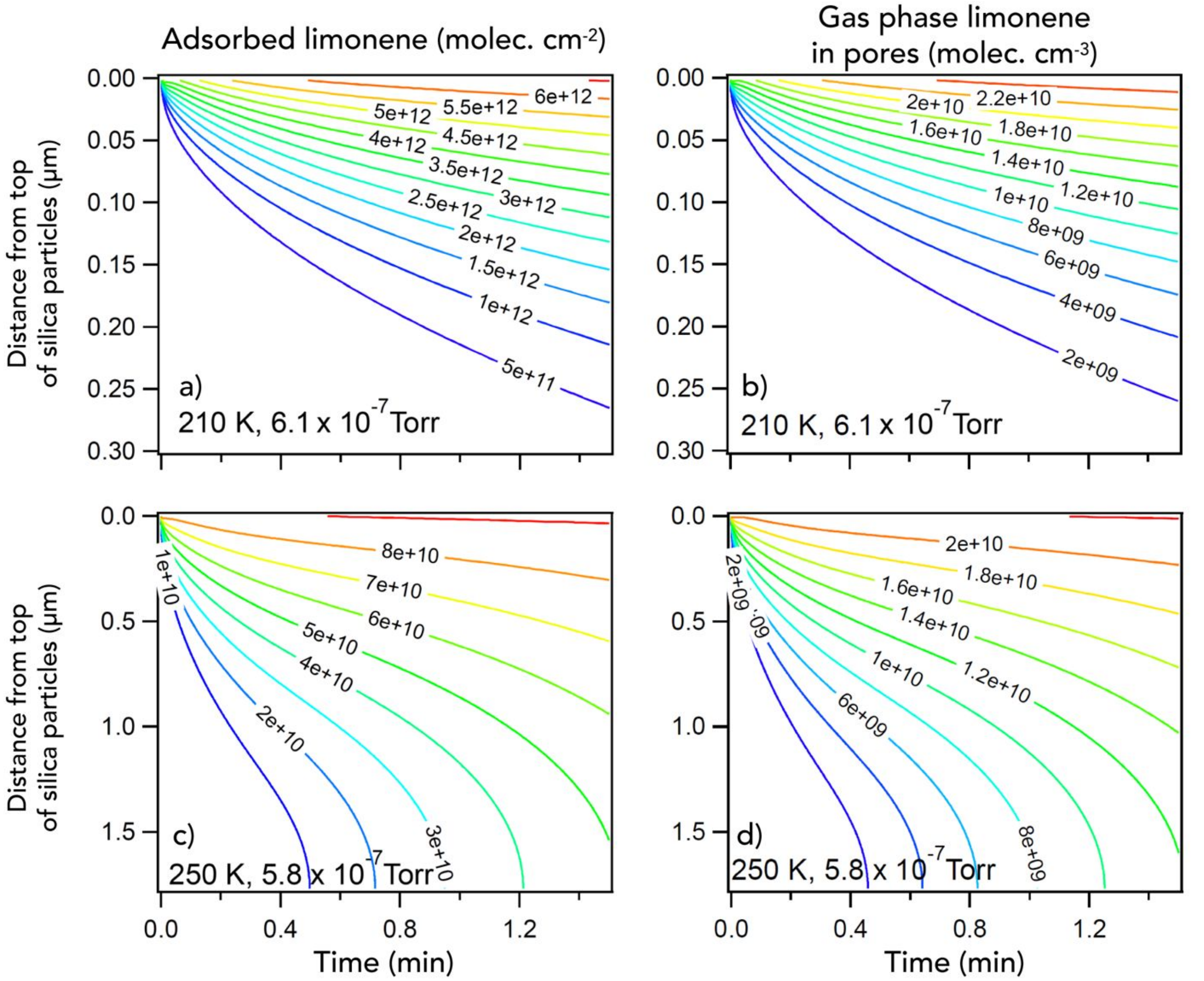

Figure 7. Kinetic multilayer model predictions of concentrations of limonene in the gas phase and on the silica particle surfaces, as a function of time and depth into the particle bed. (a, c) adsorbed limonene (molecule cm^{-2}) at 210 and 250 K; (b, d) gas-phase limonene in pores at 210 and 250 K respectively. Pressures indicate limonene gas pressure prior to opening sample lid. (Note the difference in vertical axis scale between top and bottom rows.)